



# Ultralow-content Pd in-situ incorporation mediated hierarchical defects in corner-etched Cu<sub>2</sub>O octahedra for enhanced electrocatalytic nitrate reduction to ammonia

You Xu, Kaili Ren, Tianlun Ren, Mingzhen Wang, Ziqiang Wang, Xiaonian Li, Liang Wang\*,  
Hongjing Wang\*

State Key Laboratory Breeding Base of Green-Chemical Synthesis Technology, College of Chemical Engineering, Zhejiang University of Technology, 18 Chaowang Road, Hangzhou, Zhejiang 310014, PR China

## ARTICLE INFO

**Keywords:**  
Pd-Cu<sub>2</sub>O  
Hierarchical defects  
Nitrate electroreduction  
Ammonia synthesis  
Conner-etched octahedra

## ABSTRACT

Electrochemical reduction of nitrate (NO<sub>3</sub><sup>-</sup>) to ammonia (NH<sub>3</sub>) offers a sustainable avenue to close the NO<sub>3</sub><sup>-</sup> cycle for NH<sub>3</sub> synthesis. Critical to the feasibility of electrochemical NO<sub>3</sub><sup>-</sup>-to-NH<sub>3</sub> technology is the development of cost-effective, scalable and selective catalysts that can produce NH<sub>3</sub> with high yield. To this end, we design and construct ultralow-content Pd (2.93 at%) in-situ incorporated Cu<sub>2</sub>O corner-etched octahedra (Pd-Cu<sub>2</sub>O CEO) with cavity and oxygen vacancy defects for selectively electrochemical NO<sub>3</sub><sup>-</sup>-to-NH<sub>3</sub> transformation. The unique corner-etched cavity structure, rich surface oxygen vacancies, and Pd-Cu<sub>2</sub>O dual active sites, synergistically promote nitrate electroreduction undergo ammonia formation reaction pathway. Impressively, the as-made Pd-Cu<sub>2</sub>O CEO exhibited outstanding activity for electrocatalytic NO<sub>3</sub><sup>-</sup>-to-NH<sub>3</sub>, with high ammonia selectivity (95.31%) and Faradaic efficiency (96.56%). The developed hierarchical-defect strategy may open a new avenue for reasonable design of defect electrocatalysts to contribute desirable properties and functionalities in specific applications.

## 1. Introduction

Ammonia (NH<sub>3</sub>) is undoubtedly a key chemical that plays an important role in agricultural, textile, plastics and pharmaceutical industries. Moreover, NH<sub>3</sub> can be used as an energy carrier for energy storage and transportation [1–4]. In industry, NH<sub>3</sub> is produced via energy-intensive Haber-Bosch process, which suffers from drawbacks of high energy consumption and high greenhouse gas emissions [5–9]. Under pressure of energy and environment, the exploration of energy-efficient and environment-friendly routes for ammonia synthesis is imperative. Nitrate contamination of water resources has become an increasing problem globally, and the leaching of nitrate from water has detrimental environmental effects, including eutrophication, global acidification, climate change and ozone layer damage in the stratosphere [10–14]. Traditional technologies for the remediation of nitrate-contaminated groundwater (e.g., membrane separation, ion exchange, chemical reduction and biological denitrification) are usually accompanied by high post-treatment costs, stringent operating conditions, and cumbersome processes [15,16]. Alternatively,

electrochemical reduction of waste nitrate (NO<sub>3</sub><sup>-</sup>) to valuable NH<sub>3</sub> offers a sustainable avenue to close the NO<sub>3</sub><sup>-</sup> cycle for NH<sub>3</sub> synthesis [9, 17–26]. On the one hand, it can effectively convert NO<sub>3</sub><sup>-</sup> into valuable NH<sub>3</sub> under the drive of renewable electricity, which can be easily recovered from its aqueous solution by means of regenerated resins [27–31]. On the other hand, the process of nitrate electroreduction can potentially be integrated with other attractive electrochemical reactions (e.g., CO<sub>2</sub> electroreduction) to produce other high value-added chemicals [32–34].

Electrochemical nitrate-to-ammonia transformation is a complicated multi-electron-transfer process [35–37]. In this complex transformation process, some undesired by-products, such as nitrogen-oxygen anion and dinitrogen, are inevitably produced, resulting in low ammonia selectivity [38–41]. Simultaneously, the hydrogen evolution reaction (HER) is the main competing reaction at high potentials, which severely reduces the ammonia yield and Faradaic efficiency (FE) [42,43]. Therefore, critical to the feasibility of electrochemical nitrate-to-ammonia technology is the development of cost-effective, scalable and selective catalysts that can produce ammonia with high

\* Corresponding authors.

E-mail addresses: [wangliang@zjut.edu.cn](mailto:wangliang@zjut.edu.cn) (L. Wang), [hjw@zjut.edu.cn](mailto:hjw@zjut.edu.cn) (H. Wang).



yield. In this regard, Cu and Cu-based nanomaterials are highly active for nitrate electroreduction due to the similarity energy levels between Cu's d-orbital and nitrate's LUMO  $\pi^*$  molecular orbital [44–48]. For achieving higher catalytic efficiency, the catalysts can be molded into specific morphologies/structures. Among various nanostructures, polyhedral nanocrystals with engraved surfaces generally exhibit novel physicochemical properties, such as increasing specific surface areas and enriching catalytically active sites, superior to those of smooth surfaces [49,50]. Meanwhile, rationally engineering of structural defects (e.g., oxygen vacancy) in catalysts can tune the adsorption of oxygen-containing intermediates on the surface of the catalyst by adjusting the electronic structure around the metal ions, and the resulting unsaturated coordination structure can endow the catalyst with abundant active sites [51,52].

Based on the above considerations, herein, we designed and constructed ultralow-content Pd (2.93 at%) in-situ incorporated Cu<sub>2</sub>O conner-etched octahedra (Pd-Cu<sub>2</sub>O CEO) with cavity and oxygen vacancy defects by a hierarchical-defect strategy, in which the incorporation of Pd could induce the formation of conner-etched octahedra structure (cavity defects) and mediate surface oxygen vacancy defects. In such a dual active sites (Pd and Cu<sub>2</sub>O) system, part of Cu<sub>2</sub>O is electrochemically reduced to metallic Cu and the in-situ generated Cu<sup>+</sup>/Cu<sup>0</sup> serves as active species for nitrate electroreduction. Meanwhile, the Pd sites can provide active centers for the adsorption of H ion and the formed Pd-H intermediates can promote the formation of the target product ammonia via catalytic hydrogenation. Notably, the synergistic action of cavity and oxygen vacancy defects plays a remarkable role in promoting the adsorption of nitrates, weakening the N-O bond, and inhibiting the formation of by-products. Benefiting from these advantages, the Pd-Cu<sub>2</sub>O CEO show outstanding activity for electrocatalytic NO<sub>3</sub><sup>-</sup>-to-NH<sub>3</sub> transformation, with a NH<sub>3</sub> yield of 925.11  $\mu\text{g h}^{-1} \text{mg}_{\text{cat}}^{-1}$ , a NH<sub>3</sub> selectivity of 95.31%, and a NH<sub>3</sub> FE of 96.56%.

## 2. Experimental section

### 2.1. Chemicals

Copper(II) sulfate pentahydrate(CuSO<sub>4</sub>·5H<sub>2</sub>O, ≥ 99.0%) was purchased from Lingfeng Chemical Reagent Industrial Corporation (Shanghai, China). Glucose anhydrous (C<sub>6</sub>H<sub>12</sub>O<sub>6</sub>, ≥ 99.7%), potassium sodium tartrate tetrahydrate (C<sub>4</sub>H<sub>4</sub>O<sub>6</sub>KNa·4H<sub>2</sub>O, 99.0%), potassium hydroxide (KOH, 90.0%), palladium chloride (PdCl<sub>2</sub>, 59–60%), ammonium chloride (NH<sub>4</sub>Cl), ammonium chloride-<sup>15</sup>N (<sup>15</sup>NH<sub>4</sub>Cl), phosphoric acid, *p*-aminobenzenesulfonamide, sulfamic acid, Nessler's reagent, *N*-(1-Naphthyl) ethylenediamine dihydrochloride, potassium sodium tartrate, potassium nitrate (KNO<sub>3</sub>), potassium nitrate-<sup>15</sup>N (K<sup>15</sup>NO<sub>3</sub>) and potassium sulfate (K<sub>2</sub>SO<sub>4</sub>) were obtained from Aladdin Industrial Corporation (Shanghai, China). Concentrated hydrochloric acid and ethanol (C<sub>2</sub>H<sub>5</sub>OH) were purchased from Beijing Chemical Works. Nafion (5 wt %) solution were purchased from Sigma-Aldrich.

### 2.2. Synthesis of Pd-Cu<sub>2</sub>O CEO

The Pd-Cu<sub>2</sub>O CEO were synthesized by procedure developed by Chen et al. [49], with some modifications by changing the concentrations of PdCl<sub>2</sub> and glucose in the mixed reaction solution. First, an alkaline copper tartrate complex solution (250 mL) containing CuSO<sub>4</sub> (2.8 mM), C<sub>4</sub>H<sub>4</sub>O<sub>6</sub>KNa (8.9 mM) and KOH (8 mM) was prepared. Subsequently, 4.8 mg of PdCl<sub>2</sub> and a 10 mL of 0.25 M glucose solution were added into to the above copper tartrate complex solution, followed by sonicating for 5 min to yield a light blue solution. Then, the solution was stirred vigorously in a 75 °C water bath for 2.5 h. The final product was collected by centrifugation, washed several times with water and ethanol, then dried in a 50 °C vacuum oven for 10 h. The Cu<sub>2</sub>O octahedra were synthesized by similar procedure except for the absence of PdCl<sub>2</sub>.

### 2.3. Characterization

The microstructure of all samples was taken by scanning electron microscopy (SEM, ZEISS Gemini 500). The transmission electron microscopy (FEI Talos-S) was used to test transmission electron microscopy (TEM), high-resolution TEM (HRTEM), selected area electron diffraction (SAED), high-angle annular dark field-scanning TEM (HAADF-STEM), and energy dispersive X-ray spectroscopy (EDX) mapping images at an acceleration voltage of 200 kV. The composition of the catalysts was analyzed by an inductively coupled plasma-optical emission spectrometry (ICP-OES, PerkinElmer Optima 8300). Electron paramagnetic resonance (EPR) measurements were carried out on a Bruker EMXPLUS. The superconducting-magnet NMR spectrometer (Bruker AVANCE III HD 500 MHz) was used to test 1 H nuclear magnetic resonance (NMR) spectra. X-ray diffraction (XRD) characterization was received by PANalytical X'Pert PRO equipped with a Cu K $\alpha$  radiation. X-ray photoelectron spectroscopy (XPS) date were executed utilizing a microprobe Spectrometer (ULVAC PHI Quantera) with Al K $\alpha$  radiation. TU-1900 spectrophotometer was used to measurement UV-vis absorption spectra.

### 2.4. Electrochemical measurements

The CHI 660E electrochemical workstation was used to perform electrochemical measurements in a H-type electrolytic cell with a three-electrode system composed of a saturated calomel electrode (SCE) (reference electrode), a Pt foil (counter electrode) and a catalyst-decorated carbon paper (CP) (working electrode). Before using for preparing the working electrode, the carbon paper was soaked in 3 M HCl for 15 min, and then washed three times with water and ethanol, respectively. For preparing the catalyst ink, 5 mg of as-prepared Pd-Cu<sub>2</sub>O CEO and 20  $\mu\text{L}$  of 5 wt% Nafion solution dissolved in a mixture of water (490  $\mu\text{L}$ ) and ethanol (490  $\mu\text{L}$ ) under sonication. Then, 200  $\mu\text{L}$  of catalyst ink was dropped on carbon paper substrate ( $1 \times 1 \text{ cm}^2$ ) and dried in a 60 °C vacuum oven, forming the working electrode (catalyst loading: 1 mg  $\text{cm}^{-2}$ ). When performing nitrate electroreduction measurements, 0.5 M K<sub>2</sub>SO<sub>4</sub> solution with and without 50 ppm KNO<sub>3</sub> were used as cathode electrolyte and anode electrolyte, respectively. Before performing chronoamperometry test on different potentials, the linear scanning voltammetry (LSV) is repeated at a rate of 10 mV  $\text{s}^{-1}$  until the curves basically coincide and the electrolyte was purged using pure Ar (99.99%) for 30 min. Chronoamperometry was tested at specific applied potentials with a stirring rate of 500 rpm for 2 h. Electrochemical impedance spectroscopy (EIS) was conducted in a 0.5 M K<sub>2</sub>SO<sub>4</sub> solution containing 50 ppm KNO<sub>3</sub> at –1.1 V (vs. SCE), with the frequency range of 0.1 Hz ~100 kHz and the AC amplitude of 5 mV. In this study, the current density data were obtained by normalizing the current to the geometric area of carbon paper substrate. Details about qualitative and quantitative analysis of nitrate electroreduction products can be found in [Supplementary Material](#).

## 3. Results and discussion

### 3.1. Synthesis and characterization of Pd-Cu<sub>2</sub>O CEO

Uniform Pd-Cu<sub>2</sub>O CEO were prepared through a one-pot solution synthetic strategy, as schematically illustrated in [Fig. 1](#). In the initial stage, PdCl<sub>2</sub> is first reduced by glucose to generate Pd(0) seeds, which then could catalyze the reductive transformation of Cu<sup>2+</sup>-tartrate complex to Cu<sub>2</sub>O octahedra with glucose. Subsequently, these Cu<sub>2</sub>O octahedra evolved into corner-etched Cu<sub>2</sub>O octahedra through a Pd(0)-catalyzed, oxygen-engaged oxidation process [53]. During the whole process, low content of Pd was incorporated into the Cu<sub>2</sub>O structure, as evidenced by later characterization. The introduction of Pd into Cu<sub>2</sub>O structure can favor the formation of oxygen vacancies by reducing its formation energy, as also demonstrated by other Pd/oxide systems

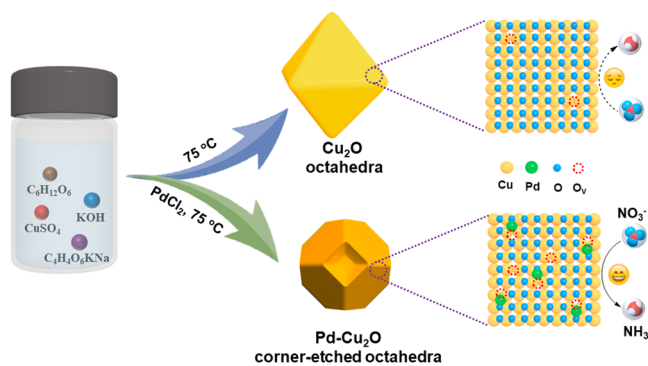


**Fig. 1.** Schematic illustration of the synthesis process of the Pd-Cu<sub>2</sub>O CEO and Cu<sub>2</sub>O octahedra.

[54–56]. In the absence of PdCl<sub>2</sub> precursor, Cu<sub>2</sub>O octahedra with larger size (around 600 nm) were generated (Fig. S1).

Information about morphology and structure for the as-prepared Pd-Cu<sub>2</sub>O CEO were acquired by means of SEM and TEM characterization. A typical SEM image of Pd-Cu<sub>2</sub>O CEO is shown in Fig. 2a, where uniform octahedral structures with abundant corner-etched cavities can be clearly seen. The well-etched cavity structure can also be observed in the TEM images (Fig. 2b and c), and the particle size of the corner-etched octahedra is about 400 nm. From the HRTEM image (Fig. 2d), the fringes with a lattice spacing of 0.296 nm attribute to the (110) planes of Cu<sub>2</sub>O. Remarkably, the HAADF-STEM image and corresponding elemental mapping on a Pd-Cu<sub>2</sub>O corner-etched octahedron proves the existence of Cu, Pd and O elements and shows these three elements are distributed homogenously on the corner-etched octahedron's surface (Fig. 2e). ICP-OES analysis reveals an atomic ratio of 2.93% for Pd in the Pd-Cu<sub>2</sub>O CEO structure, which is roughly consistent with the EDX result (2.33 at%, Fig. S2).

To get insight into the crystal structure and composition, XRD and XPS were performed on the as-synthesized Pd-Cu<sub>2</sub>O CEO. Fig. 3a shows

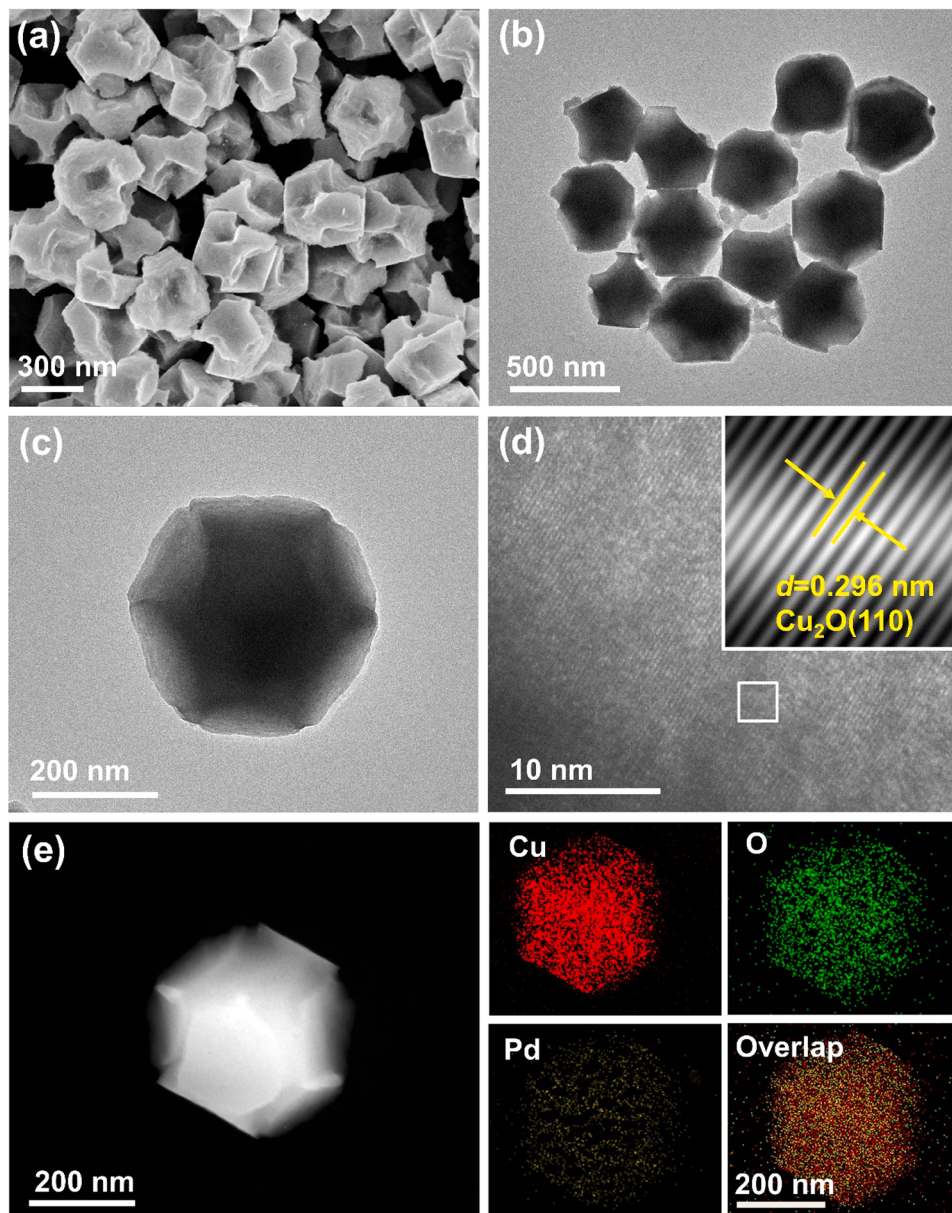


**Fig. 2.** (a) SEM image, (b and c) TEM images, (d) HRTEM image, (e) HAADF-STEM image and EDX elemental mapping images of the Pd-Cu<sub>2</sub>O CEO.

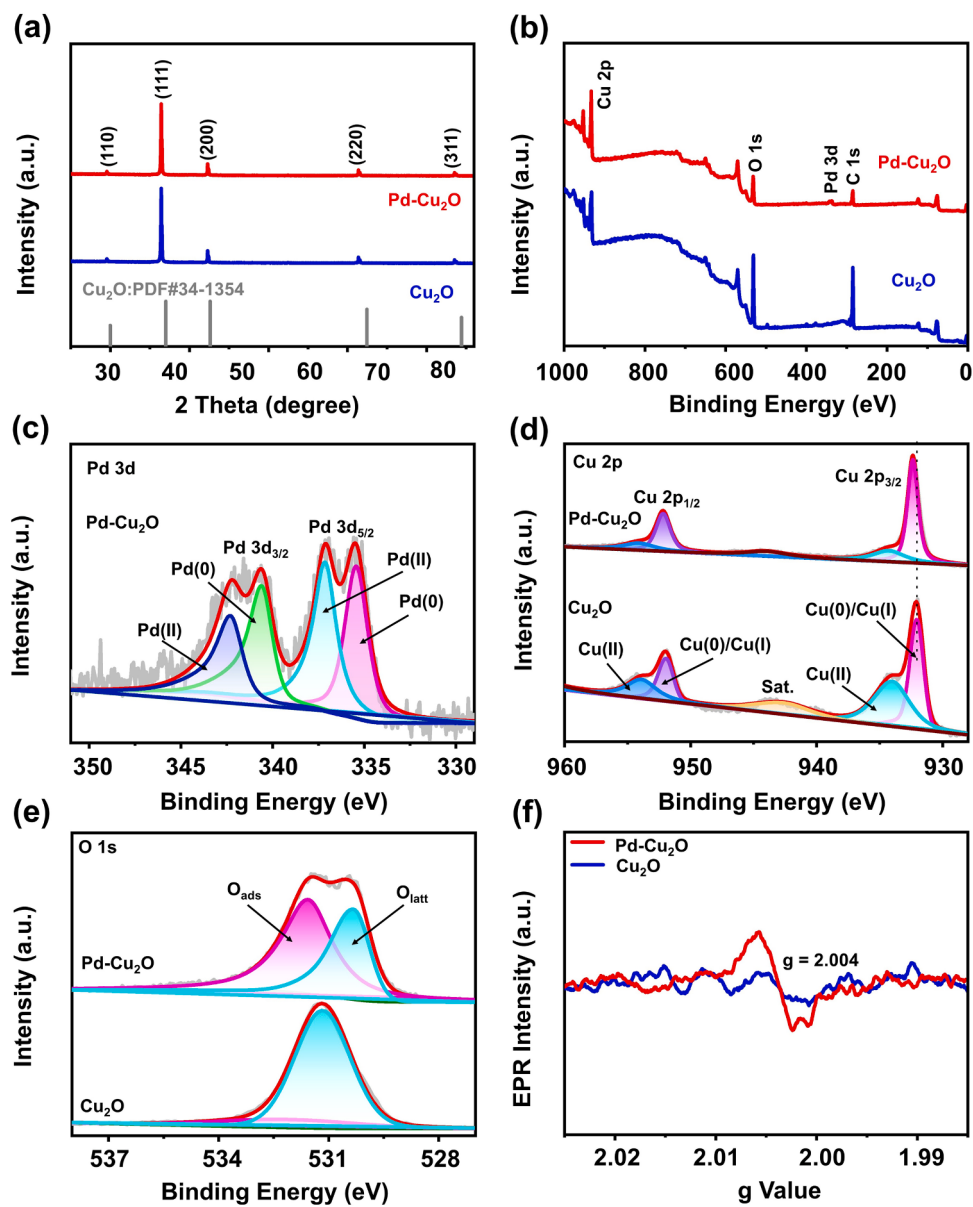


**Fig. 3.** (a) XRD patterns, (b) XPS survey spectra, (c) Pd 3d XPS spectrum, (d) Cu 2p XPS spectra, (e) O 1s XPS spectra and (f) EPR spectra of as-synthesized Pd-Cu<sub>2</sub>O CEO and Cu<sub>2</sub>O octahedra.

XRD pattern of Pd-Cu<sub>2</sub>O CEO, demonstrating cubic-structured Cu<sub>2</sub>O crystals (PDF#34-1354), similar to the pure Cu<sub>2</sub>O octahedra. The absence of diffraction peaks for Pd is due to the low-content of Pd and the incorporation of Pd into Cu<sub>2</sub>O structure. The existence of Cu, O and Pd elements is further evidenced by the XPS survey spectrum (Fig. 3b). As shown in Fig. 3c, high-resolution XPS patterns of Pd 3d can be fitted into four peaks: Pd (0) 3d<sub>5/2</sub> at 335.4 eV, Pd (0) 3d<sub>3/2</sub> at 340.6 eV, Pd (II) 3d<sub>5/2</sub> at 337.1 eV, and Pd (II) 3d<sub>3/2</sub> at 342.3 eV [57,58]. As for the Cu 2p XPS spectrum of Pd-Cu<sub>2</sub>O CEO (Fig. 3d), the binding energies at 932.4 eV and 952.2 eV can be labeled as Cu (0 or I) 2p<sub>3/2</sub> and Cu (0 or I) 2p<sub>1/2</sub>, respectively. Meanwhile, the two weak peaks at 934.3 eV and 954.2 eV respond to Cu (II) 2p<sub>3/2</sub> and Cu (II) 2p<sub>1/2</sub>, and a Cu 2p satellite peak can be fitted at 944.1 eV [59]. Compared with the pure Cu<sub>2</sub>O octahedra, the Cu (0 or I) 2p<sub>3/2</sub> peak in Pd-Cu<sub>2</sub>O CEO show slightly positive shift, indicative of electronic interaction between Cu<sub>2</sub>O and Pd [60]. In the XPS spectrum of O 1s (Fig. 3e), two peaks at 530.3 eV and 531.6 eV belonged to lattice oxygen (O<sub>latt</sub>) and surface-adsorbed oxygen (O<sub>ads</sub>) [61], respectively. Obviously, the content of O<sub>ads</sub> in the Pd-Cu<sub>2</sub>O CEO is much higher than that in pure Cu<sub>2</sub>O octahedra. According to

literature, the content of O<sub>ads</sub> oxygen species can reflect the concentration of surface oxygen vacancies because they can only be absorbed at oxygen vacancies [62,63]. Thus, more surface oxygen vacancies should occur on the sample with higher O<sub>ads</sub> species content. The EPR technology is performed to further substantiate the presence of oxygen vacancies in Pd-Cu<sub>2</sub>O CEO. As shown in Fig. 3f, at approximately  $g = 2.004$ , the Pd-Cu<sub>2</sub>O CEO exhibit a stronger EPR signal compared with Cu<sub>2</sub>O, suggesting that oxygen vacancies are enriched in the Pd-Cu<sub>2</sub>O CEO [64,65]. All above characterization results indicate that Pd-Cu<sub>2</sub>O CEO with hierarchical cavity and oxygen vacancy defects are successfully prepared successfully by a one-pot catalytic self-templating route.

### 3.2. Electrocatalytic performance for nitrate-to-ammonia conversion

Inspired by the attractive catalytic properties of other defect electrocatalysts, we evaluated the electrocatalytic nitrate-to-ammonia activity of the as-synthesis Pd-Cu<sub>2</sub>O CEO. Electrochemical measurements were conducted in an H-type electrolytic cell (Fig. S3). LSV was first carried out in 0.5 M K<sub>2</sub>SO<sub>4</sub> electrolyte solution with and without KNO<sub>3</sub>

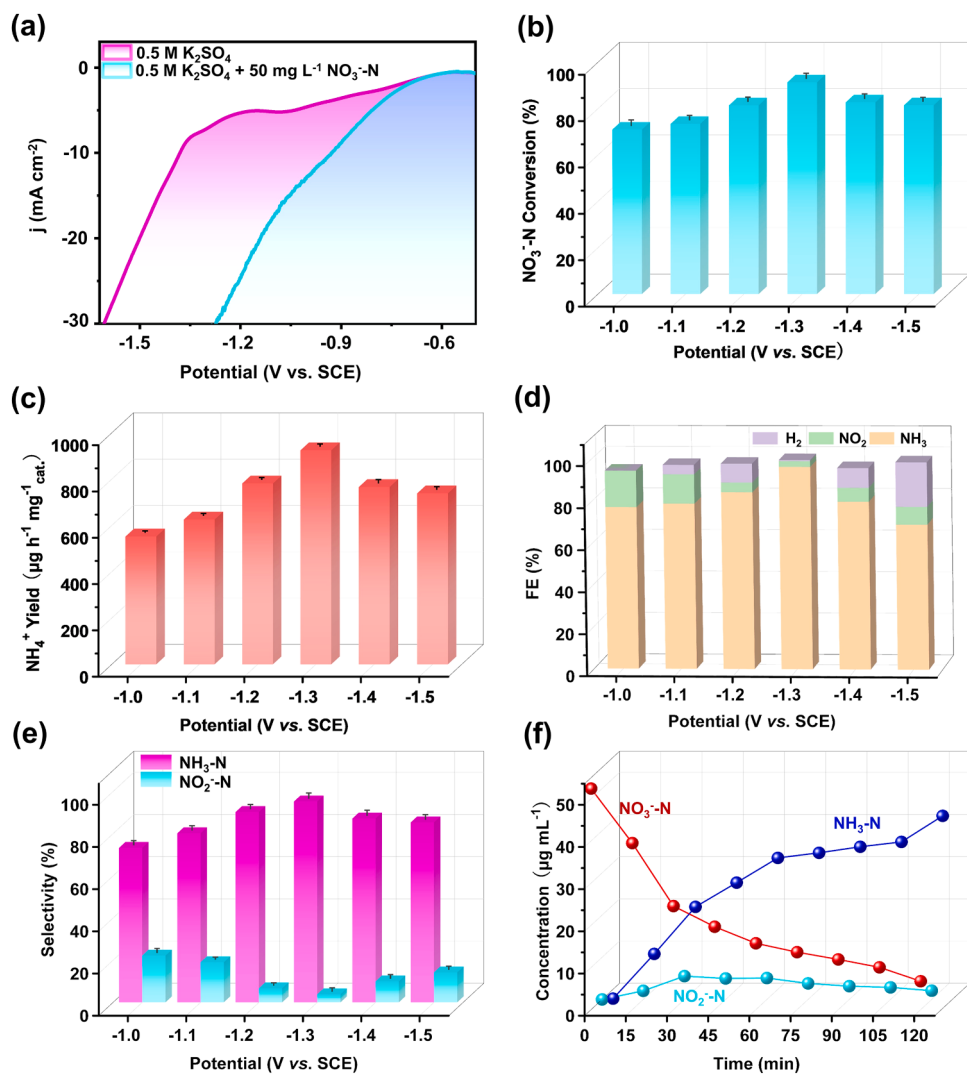


**Fig. 4.** (a) LSV curves of the Pd-Cu<sub>2</sub>O CEO in 0.5 M K<sub>2</sub>SO<sub>4</sub> with or without 50 ppm KNO<sub>3</sub>. (b) NO<sub>3</sub><sup>-</sup>-N conversion rate, (c) NH<sub>3</sub> yield, (d) FEs of NH<sub>3</sub>, NO<sub>2</sub><sup>-</sup> and H<sub>2</sub>, (e) NH<sub>3</sub>-N and NO<sub>2</sub><sup>-</sup>-N selectivities of the Pd-Cu<sub>2</sub>O CEO at different potentials for 2 h. (f) The NO<sub>3</sub><sup>-</sup>-N, NO<sub>2</sub><sup>-</sup>-N and NH<sub>3</sub>-N concentration versus different reaction time of the Pd-Cu<sub>2</sub>O CEO at -1.3 V vs. SCE.

(50 ppm), respectively, to evaluate the electrocatalytic response of Pd-Cu<sub>2</sub>O CEO catalyst toward nitrate electroreduction. As presented in Fig. 4a, much higher current density was reached on the Pd-Cu<sub>2</sub>O CEO in the presence of KNO<sub>3</sub>, suggesting the Pd-Cu<sub>2</sub>O CEO could catalyze the nitrate electroreduction. The electrocatalytic properties for nitrate conversion on the Pd-Cu<sub>2</sub>O CEO were studied at different applied potentials from -1.0 to -1.5 V vs. SCE. Concentrations of NO<sub>3</sub><sup>-</sup>-N, NO<sub>2</sub><sup>-</sup>-N and NH<sub>3</sub>-N in the electrolyte are determined by UV-vis spectrophotometry and then calculated by crossing the calibration curves (Figs. S4–S6). The NO<sub>3</sub><sup>-</sup> conversion rate, NH<sub>3</sub> yield rate and NH<sub>3</sub> FE over the Pd-Cu<sub>2</sub>O CEO display volcano-shaped curves (Fig. 4b-d), with the maximum values achieved at -1.3 V vs. SCE (NO<sub>3</sub><sup>-</sup> conversion rate: 91.36%, NH<sub>3</sub> yield rate: 925.11 μg h<sup>-1</sup> mg<sup>-1</sup> cat., and NH<sub>3</sub> FE: 96.56%). The FE for NO<sub>2</sub><sup>-</sup>-N and H<sub>2</sub> at -1.3 V vs. SCE are only 2.8% and 0.5%, respectively. Moreover, as shown in Fig. 4e, the selectivity of NH<sub>3</sub>-N reaches 95.31% at -1.3 V vs. SCE, while the selectivity of by-product NO<sub>2</sub><sup>-</sup>-N is only 4.55% at the same conditions. When the applied potentials are more negative than -1.3 V vs. SCE, the nitrate-to-ammonia activity decreases mainly due to the competitive HER. Fig. 4f shows the concentration-time variation curves of NH<sub>3</sub>-N, NO<sub>3</sub><sup>-</sup>-N and NO<sub>2</sub><sup>-</sup>-N during electroreduction process at -1.3 V vs. SCE. When the electroreduction reaction proceeded for 2 h, 91.4% of NO<sub>3</sub><sup>-</sup>-N has been reduced, accompanied by increasing concentration of NH<sub>3</sub>-N, yielding

43.53 μg mL<sup>-1</sup> after 2 h's reaction. Significantly, the concentration of NO<sub>2</sub><sup>-</sup>-N fluctuates in a low-level range within 2 h, which implies that the Pd-Cu<sub>2</sub>O CEO has high selectivity for NH<sub>3</sub> production. Impressively, the electrocatalytic nitrate-to-ammonia activity over the Pd-Cu<sub>2</sub>O CEO is superior to most of reported catalysts (Table S1).

The recyclability of the Pd-Cu<sub>2</sub>O CEO towards nitrate electroreduction was evaluated by consecutive cycles at -1.3 V vs. SCE. As shown in Fig. 5a-c, the NO<sub>3</sub><sup>-</sup>-N conversion rate, NH<sub>3</sub> yield rate and NH<sub>3</sub> FE are stable after eight consecutive recycling potentials using the same catalyst. Moreover, the catalyst after stability testing still maintain the initial corner-etched octahedral structure (Fig. S7), indicating the well microstructure stability of the catalysts. Considering that Cu<sub>2</sub>O may be unstable and easily electrochemically reduced in the electrocatalytic process, to explore the actual active species, XRD and XPS were further performed to analyse the phase structure and surface composition of the post-test Pd-Cu<sub>2</sub>O CEO. Fig. S8a shows XRD pattern of Pd-Cu<sub>2</sub>O CEO after nitrate electroreduction testing. The three diffraction peaks corresponding to Cu (PDF#04-0836) at 43.7°, 50.7° and 74.5° can be noticed, which is different from the pure cubic-structured Cu<sub>2</sub>O crystals (PDF#34-1354) in fresh Pd-Cu<sub>2</sub>O CEO, suggesting the existence of metallic Cu species. At the same time, some the diffraction peaks of Cu<sub>2</sub>O (PDF#35-1091) are also present, indicating that Cu<sub>2</sub>O is not completely converted into metallic Cu and the partial oxidation state is maintained.

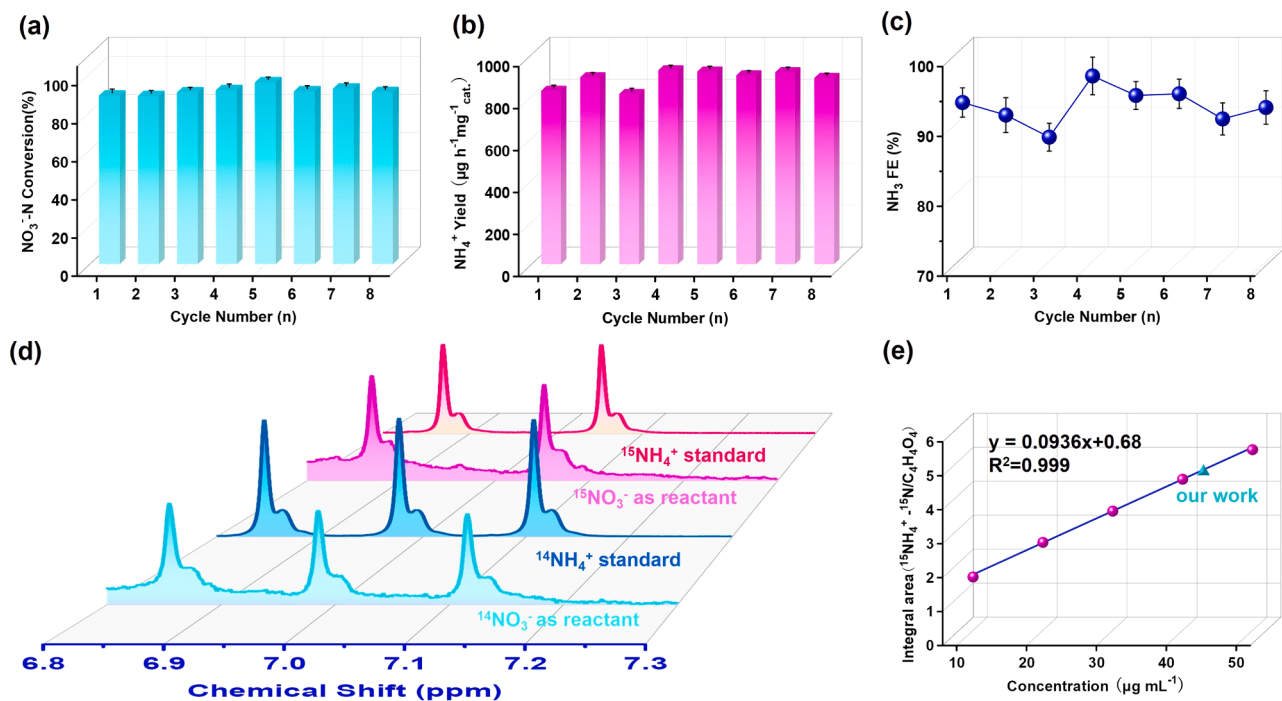


**Fig. 5.** (a)  $\text{NO}_3^-$ -N conversion rate, (b)  $\text{NH}_3$  yield rate, and (c)  $\text{NH}_3$  FE of cycling eight times for the Pd-Cu<sub>2</sub>O CEO at  $-1.3$  V vs. SCE. (d)  $^1\text{H}$  NMR spectra of  $^{15}\text{NH}_4^+$  calibration solution,  $^{14}\text{NH}_4^+$  calibration solution and the electrolyte after nitrate electroreduction using  $^{15}\text{NO}_3^-$  and  $^{14}\text{NO}_3^-$  as the nitrogen source. (e) The standard curve of integral area ( $^{15}\text{NH}_4^+ \cdot ^{15}\text{N}/\text{C}_4\text{H}_4\text{O}_4$ ) against  $^{15}\text{NH}_4^+ \cdot ^{15}\text{N}$  concentration.

High-resolution XPS patterns of Pd 3d can be fitted to four peaks (Fig. S8b). The peaks at 335.2 eV and 340.6 eV can be indexed to Pd (0) 3d<sub>5/2</sub> and Pd (0) 3d<sub>3/2</sub>, while the fitted peaks for Pd (II) 3d<sub>5/2</sub> and Pd (II) 3d<sub>3/2</sub> can be observed at the binding energy 337.5 eV and 342.8 eV. The XPS spectra of Cu 2p shows two major peaks at 932.2 eV (Cu 2p<sub>3/2</sub>) and 952.1 eV (Cu 2p<sub>1/2</sub>) in Fig. S8c. The binding energy at 932.2 eV and 952.1 eV can be labeled as Cu (0 or I) 2p<sub>3/2</sub> and Cu (0 or I) 2p<sub>1/2</sub>, respectively. The two peaks at 933.3 eV and 953.4 eV respond to Cu (II) 2p<sub>3/2</sub> and Cu (II) 2p<sub>1/2</sub>, and a Cu 2p satellite peak can be fitted at 944.8 eV. Apparently, the contents of Cu (II) and Pd (II) species are significantly reduced relative to the fresh Pd-Cu<sub>2</sub>O CEO after electrochemical reduction. In the XPS spectrum of O 1s (Fig. S8d), compared with freshly prepared Pd-Cu<sub>2</sub>O CEO, the O<sub>ads</sub> peak intensity of post-test Pd-Cu<sub>2</sub>O CEO is significantly weakened, suggesting the decrease of surface oxygen vacancy defects. The characterization results combined with XRD and XPS confirm that the in-situ electrochemical conversion from Pd-Cu<sub>2</sub>O to Pd-Cu/Cu<sub>2</sub>O, which is served as the active phase in the actual catalytic process.

In order to confirm the source of ammonia produced,  $^{15}\text{N}$  isotopic labeling experiments are performed. The  $\text{NH}_3$  concentration in liquid products was also determined quantitatively by  $^1\text{H}$  NMR. As displayed in Fig. 5d, the  $^1\text{H}$  NMR spectrum of the electrolyte using  $\text{K}^{15}\text{NO}_3$  as reactant shows a double peak typical of  $^{15}\text{NH}_4^+$ . In comparison, the  $^1\text{H}$  NMR spectrum of the electrolyte using  $\text{K}^{14}\text{NO}_3$  as reactant shows a triple peak typical of  $^{14}\text{NH}_4^+$ . Maleic acid ( $\text{C}_4\text{H}_4\text{O}_4$ ) has been selected as the  $^1\text{H}$  NMR external standard to perform quantitative tests (Fig. S9). Based on the standard curve of the integrated area ( $\text{NH}_4^+ \cdot \text{N}/\text{C}_4\text{H}_4\text{O}_4$ ) relative to the  $\text{NH}_4^+ \cdot \text{N}$  concentration (Fig. 5e), the quantification of the generated  $^{15}\text{NH}_4^+ \cdot ^{15}\text{N}$  is calculated, and is very close to the  $^{14}\text{NH}_4^+ \cdot ^{14}\text{N}$  by the colorimetric method. The above results provide strong evidence that the  $\text{NH}_3$  obtained in electrolyte is from the nitrate electroreduction.

### 3.3. Mechanism analysis

To further investigate the influence of cavity and oxygen vacancy defects on the nitrate-to-ammonia activity, the electrocatalytic

performance of the comparative sample (Cu<sub>2</sub>O octahedra with poor oxygen vacancies) is measured under the same conditions. It is observed from the LSV curves that the current density of Pd-Cu<sub>2</sub>O CEO is significantly higher than that of Cu<sub>2</sub>O during the nitrate reduction measurements (Fig. 6a). The performance of Cu<sub>2</sub>O for nitrate electroreduction is evaluated at  $-1.3$  V vs. SCE. It is clear from Fig. 6b that the  $\text{NO}_3^-$ -N conversion rate,  $\text{NH}_3$  selectivity,  $\text{NH}_3$  FE and  $\text{NH}_3$  yield rate of Pd-Cu<sub>2</sub>O CEO are all higher than those of Cu<sub>2</sub>O (62.14%, 58.73%, 49.11%,  $352.5 \mu\text{g h}^{-1} \text{ mg}_{\text{cat}}^{-1}$ ), while the  $\text{NO}_2^-$ -N selectivity (5.55%) is significantly lower than that of Cu<sub>2</sub>O (41%). In addition, the low  $\text{NH}_3$  yield rate is obtained by using bare CP as the electrode, indicating that the catalytic activity is mainly derived from Pd-Cu<sub>2</sub>O CEO (Fig. 6c). The test results of Pd-Cu<sub>2</sub>O CEO in the electrolyte without  $\text{KNO}_3$  exclude the effect of the external environment on the experimental results (Fig. 6d). As can be seen from Fig. S10, Pd-Cu<sub>2</sub>O CEO show a higher double layer capacitance ( $C_{\text{dl}}$ ) value ( $6.28 \text{ mF cm}^{-2}$ ) than Cu<sub>2</sub>O ( $2.87 \text{ mF cm}^{-2}$ ). It is generally accepted that a higher  $C_{\text{dl}}$  value suggests a higher electrochemically active surface area (ECSA) [66–68]. Increase in ECSA in the Pd-Cu<sub>2</sub>O CEO can be attributed to the unique angle-etched cavities and oxygen vacancies, which provides large void space for efficient mass transport and highly accessible active sites for reactant adsorption (e.g.,  $\text{NO}_3^-$ ,  $\text{H}_2\text{O}$ ). EIS measurements proved the smaller charge transfer resistance of Pd-Cu<sub>2</sub>O than Cu<sub>2</sub>O (Fig. S11). As previously demonstrated both experimentally and theoretically in the literature that oxygen vacancies in defect electrocatalysts could weaken the N–O bonding of nitrate due to the oxygen atom in nitrate fill in oxygen vacancy sites [64, 69]. Moreover, Pd serves as active sites for cathodic discharge of  $\text{H}_2\text{O}$  molecules, which could generate active adsorbed hydrogen atoms ( $\text{H}_{\text{ads}}$ ) as hydrogenation species [70, 71].

On the basis of the aforementioned results and previous reports [37, 48], the nitrate-to-ammonia reaction pathway in Pd-Cu<sub>2</sub>O CEO can be described into a series of deoxidation and hydrogenation steps (Fig. 6e): (i)  $\text{NO}_3^-$  anions are targeted adsorbed on the surface oxygen vacancies to form  $\text{NO}_{3\text{(ads)}}$ . (ii) Cu<sub>2</sub>O is partially in-situ reduced to Cu/Cu<sub>2</sub>O at reductive potentials, which serves as an active phase for  $\text{NO}_3^-$  activation. As demonstrated by previous reports, electron transfer at the interface of

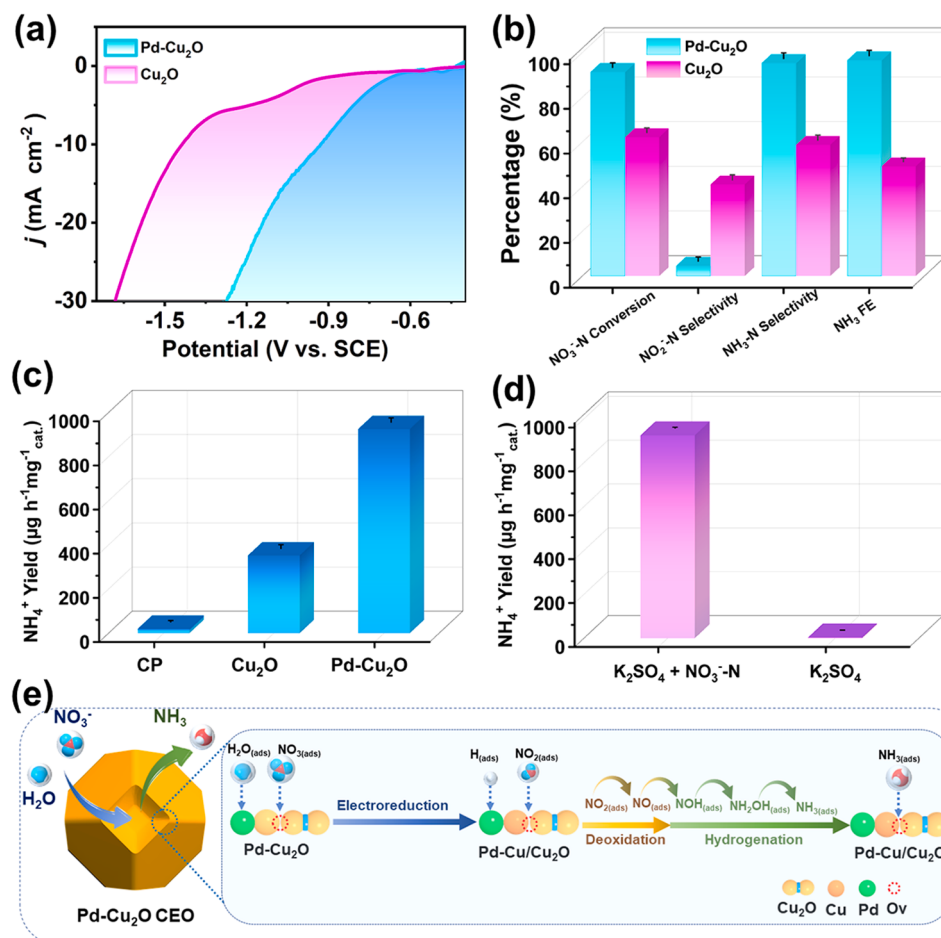


**Fig. 6.** (a) LSV curves of Pd-Cu<sub>2</sub>O CEO and Cu<sub>2</sub>O octahedra. (b) The comparisons of NO<sub>3</sub><sup>-</sup>-N conversion rate, NO<sub>2</sub>-N selectivity, NH<sub>3</sub>-N selectivity and NH<sub>3</sub> FE of Pd-Cu<sub>2</sub>O CEO and Cu<sub>2</sub>O octahedra at -1.3 V vs. SCE for 2 h. (c) NH<sub>3</sub> yield of the Pd-Cu<sub>2</sub>O CEO, Cu<sub>2</sub>O octahedra and CP. (d) NH<sub>3</sub> yield of the Pd-Cu<sub>2</sub>O CEO in 0.5 M K<sub>2</sub>SO<sub>4</sub> with and without 50 mg L<sup>-1</sup> NO<sub>3</sub><sup>-</sup>. (e) Schematic illustration showing the nitrate-to-ammonia reaction pathway over the Pd-Cu<sub>2</sub>O CEO.

Cu/Cu<sub>2</sub>O could modulate the adsorption energies of key nitrogen intermediate species [48,72]. Meanwhile, the adsorbed H<sub>2</sub>O molecules on Pd sites are reduced to form active H<sub>(ads)</sub>. (ii) NO<sub>3(ads)</sub> were reduced to NO<sub>2(ads)</sub>, which can continue to be deoxidized to form NO<sub>(ads)</sub>. (iii) Consecutive reactions between the produced NO<sub>(ads)</sub> species and H<sub>(ads)</sub> lead to form NH<sub>3(ads)</sub> via a series of hydrogenation processes and intermediates such as NOH<sub>(ads)</sub>, NH<sub>2</sub>OH<sub>(ads)</sub> [73].

#### 4. Conclusion

In conclusion, uniform Pd-Cu<sub>2</sub>O CEO with cavity and oxygen vacancy defects were successfully designed and synthesized by a hierarchical-defect strategy. The synergistic action of cavity and oxygen vacancy defects plays a remarkable role in promoting the adsorption of nitrates, weakening the N-O bond, and inhibiting the formation of by-products. Furthermore, Pd sites could afford active centers for accumulation of hydrogenated species, which facilitates the ammonia formation reaction pathway. Thus, the Pd-Cu<sub>2</sub>O CEO show outstanding electrocatalytic activity for nitrate-to-ammonia transformation. The NH<sub>3</sub> yield, NH<sub>3</sub> FE and NH<sub>3</sub>-N selectivity reach 925.11 μg h<sup>-1</sup> mg<sup>-1</sup> cat, 96.56% and 95.31%, respectively, at the optimum potential (-1.3 V vs. SCE). The study may open a new avenue for reasonable design of defect electrocatalysts with desirable properties and functionalities for ammonia electrosynthesis and beyond.

#### CRediT authorship contribution statement

**You Xu:** Investigation, Methodology, Writing – original draft. **Kaili Ren:** Formal analysis, Investigation, Data curation. **Tianlun Ren:** Data curation, Visualization, Validation. **Mingzhen Wang:** Characterization, Software. **Ziqiang Wang:** Formal analysis, Funding acquisition. **Xiaonian Li:** Resources, Conceptualization, Methodology. **Liang Wang:** Project administration, Funding acquisition, Writing – review & editing. **Hongjing Wang:** Supervision, Writing – review & editing, Funding acquisition.

#### Declaration of Competing Interest

The authors declare that they have no known competing financial interests or personal relationships that could have appeared to influence the work reported in this paper.

#### Acknowledgements

This work was financially supported by the National Natural Science Foundation of China (Nos. 21701141, 21972126, 21978264, 21905250).

#### Appendix A. Supporting information

Supplementary data associated with this article can be found in the online version at doi:10.1016/j.apcatb.2022.121094.

## References

- [1] C. Ampelli, Electrode design for ammonia synthesis, *Nat. Catal.* 3 (2020) 420–421, <https://doi.org/10.1038/s41929-020-0461-x>.
- [2] B.H.R. Suryanto, H.-L. Du, D. Wang, J. Chen, A.N. Simonov, D.R. MacFarlane, Challenges and prospects in the catalysis of electroreduction of nitrogen to ammonia, *Nat. Catal.* 2 (2019) 290–296, <https://doi.org/10.1038/s41929-019-0252-4>.
- [3] J.W. Erisman, M.A. Sutton, J. Galloway, Z. Klimont, W. Winiwarter, How a century of ammonia synthesis changed the world, *Nat. Geosci.* 1 (2008) 636–639, <https://doi.org/10.1038/ngeo325>.
- [4] Y. Guo, T. Wang, Q. Yang, X. Li, H. Li, Y. Wang, T. Jiao, Z. Huang, B. Dong, W. Zhang, J. Fan, C. Zhi, Highly efficient electrochemical reduction of nitrogen to ammonia on surface termination modified  $Ti_3C_2T_x$  MXene nanosheets, *ACS Nano* 14 (2020) 9089–9097, <https://doi.org/10.1021/acsnano.0c04284>.
- [5] M. Capdevila-Cortada, Electrifying the Haber–Bosch, *Nat. Catal.* 2 (2019) 1055–1055–1055, <https://doi.org/10.1038/s41929-019-0414-4>.
- [6] V. Kyriakou, I. Garagounis, A. Vourros, E. Vasileiou, M. Stoukides, An electrochemical Haber–Bosch process, *Joule* 4 (2020) 142–158, <https://doi.org/10.1016/j.joule.2019.10.006>.
- [7] G. Soloveichik, Electrochemical synthesis of ammonia as a potential alternative to the Haber–Bosch process, *Nat. Catal.* 2 (2019) 377–380, <https://doi.org/10.1038/s41929-019-0280-0>.
- [8] X.-W. Lv, X.-L. Liu, Y.-J. Suo, Y.-P. Liu, Z.-Y. Yuan, Identifying the dominant role of pyridinic–N–Mo bonding in synergistic electrocatalysis for ambient nitrogen reduction, *ACS Nano* 15 (2021) 12109–12118, <https://doi.org/10.1021/acsnano.1c03465>.
- [9] Y. Chen, R. Guo, X. Peng, X. Wang, X. Liu, J. Ren, J. He, L. Zhuo, J. Sun, Y. Liu, Y. Wu, J. Luo, Highly productive electrosynthesis of ammonia by admolecule-targeting single Ag sites, *ACS Nano* 14 (2020) 6938–6946, <https://doi.org/10.1021/acsnano.0c01340>.
- [10] W. Duan, G. Li, Z. Lei, T. Zhu, Y. Xue, C. Wei, C. Feng, Highly active and durable carbon electrocatalyst for nitrate reduction reaction, *Water Res.* 161 (2019) 126–135, <https://doi.org/10.1016/j.watres.2019.05.104>.
- [11] S. Guo, K. Heck, S. Kasiraju, H. Qian, Z. Zhao, L.C. Grabow, J.T. Miller, M.S. Wong, Insights into nitrate reduction over indium-decorated palladium nanoparticle catalysts, *ACS Catal.* 8 (2017) 503–515, <https://doi.org/10.1021/ascatal.7b01371>.
- [12] S. Garcia-Segura, M. Lanzarini-Lopes, K. Hristovski, P. Westerhoff, Electrocatalytic reduction of nitrate: Fundamentals to full-scale water treatment applications, *Appl. Catal. B Environ.* 236 (2018) 546–568, <https://doi.org/10.1016/j.apcatb.2018.05.041>.
- [13] R. Mao, H. Zhu, K. Wang, X. Zhao, Selective conversion of nitrate to nitrogen gas by enhanced electrochemical process assisted by reductive Fe(II)–Fe(III) hydroxides at cathode surface, *Appl. Catal. B Environ.* 298 (2021), 120552, <https://doi.org/10.1016/j.apcatb.2021.120552>.
- [14] Y.-J. Shih, Z.-L. Wu, Electroplating of surfactant-modified tin catalyst over a nickel foam electrode (Sn/Ni) for selective  $N_2$  yield from nitrate reduction as affected by Sn(200) and Sn(101) crystal facets, *Appl. Catal. B Environ.* 285 (2021), 119784, <https://doi.org/10.1016/j.apcatb.2020.119784>.
- [15] M. Duca, N. Sacré, A. Wang, S. Garbarino, D. Guay, Enhanced electrocatalytic nitrate reduction by preferentially-oriented (100) PtRh and PtIr alloys: the hidden treasures of the ‘miscibility gap’, *Appl. Catal. B Environ.* 221 (2018) 86–96, <https://doi.org/10.1016/j.apcatb.2017.08.081>.
- [16] J. Gao, B. Jiang, C. Ni, Y. Qi, Y. Zhang, N. Oturan, M.A. Oturan, Non-precious  $Co_3O_4$ – $TiO_2$ /Ti cathode based electrocatalytic nitrate reduction: preparation, performance and mechanism, *Appl. Catal. B Environ.* 254 (2019) 391–402, <https://doi.org/10.1016/j.apcatb.2019.05.016>.
- [17] H. Choi, A.W. Peters, H. Noh, L.C. Gallington, A.E. Platero-Prats, M.R. DeStefano, M. Rimoldi, S. Goswami, K.W. Chapman, O.K. Farha, J.T. Hupp, Vapor-phase fabrication and condensed-phase application of a MOF-node-supported iron thiolate photocatalyst for nitrate conversion to ammonium, *ACS Appl. Energy Mater.* 2 (2019) 8695–8700, <https://doi.org/10.1021/acsae.9b01664>.
- [18] Y. Wang, Y. Yu, R. Jia, C. Zhang, B. Zhang, Electrochemical synthesis of nitric acid from air and ammonia through waste utilization, *Natl. Sci. Rev.* 6 (2019) 730–738, <https://doi.org/10.1093/nsr/nzw019>.
- [19] T. Wu, H. Zhao, X. Zhu, Z. Xing, Q. Liu, T. Liu, S. Gao, S. Lu, G. Chen, A.M. Asiri, Y. Zhang, X. Sun, Identifying the origin of Ti(3+) activity toward enhanced electrocatalytic  $N_2$  reduction over  $TiO_2$  nanoparticles modulated by mixed-valent copper, *Adv. Mater.* 32 (2020), e2000299, <https://doi.org/10.1002/adma.202000299>.
- [20] L. Han, Z. Ren, P. Ou, H. Cheng, N. Rui, L. Lin, X. Liu, L. Zhuo, J. Song, J. Sun, J. Luo, H.L. Xin, Modulating single-atompalladium sites with copper for enhanced ambient ammonia electrosynthesis, *Angew. Chem.* 60 (2021) 345–350, <https://doi.org/10.1002/anie.202010159>.
- [21] W.J. Sun, H.Q. Ji, L.X. Li, H.Y. Zhang, Z.K. Wang, J.H. He, J.M. Lu, Built-in electric field triggered interfacial accumulation effect for efficient nitrate removal at ultra-low concentration and electroreduction to ammonia, *Angew. Chem. Int. Ed. Engl.* 60 (2021) 22933–22939, <https://doi.org/10.1002/anie.202109785.10.1002/anie.202109785>.
- [22] J.E. Kim, J.H. Jang, K.M. Lee, M. Balamurugan, Y.I. Jo, M.Y. Lee, S. Choi, S.W. Im, K.T. Nam, Electrochemical synthesis of glycine from oxalic acid and nitrate, *Angew. Chem. Int. Ed. Engl.* 60 (2021) 21943–21951, <https://doi.org/10.1002/anie.202108352>.
- [23] Y. Yao, S. Zhu, H. Wang, H. Li, M. Shao, A spectroscopic study of electrochemical nitrogen and nitrate reduction on rhodium surfaces, *Angew. Chem. Int. Ed. Engl.* 59 (2020) 10479–10483, <https://doi.org/10.1002/anie.202003071>.
- [24] Y. Li, Y.K. Go, H. Ooka, D. He, F. Jin, S.H. Kim, R. Nakamura, Enzyme mimetic active intermediates for nitrate reduction in neutral aqueous media, *Angew. Chem. Int. Ed. Engl.* 59 (2020) 9744–9750, <https://doi.org/10.1002/anie.202002647>.
- [25] P. Gao, Z.H. Xue, S.N. Zhang, D. Xu, G.Y. Zhai, Q.Y. Li, J.S. Chen, X.H. Li, Schottky barrier-induced surface electric field boosts universal reduction of  $NO_x(-)$  in water to ammonia, *Angew. Chem. Int. Ed. Engl.* 60 (2021) 20711–20716, <https://doi.org/10.1002/anie.202107858>.
- [26] A.S. Fajardo, P. Westerhoff, C.M. Sanchez-Sanchez, S. Garcia-Segura, Earth-abundant elements a sustainable solution for electrocatalytic reduction of nitrate, *Appl. Catal. B Environ.* 281 (2021), 119465, <https://doi.org/10.1016/j.apcatb.2020.119465>.
- [27] A. Thornton, P. Pearce, S.A. Parsons, Ammonium removal from solution using ion exchange on to MesoLite, an equilibrium study, *J. Hazard. Mater.* 147 (2007) 883–889, <https://doi.org/10.1016/j.jhazmat.2007.01.111>.
- [28] P.H. van Langevelde, I. Katsounaros, M.T.M. Koper, Electrocatalytic nitrate reduction for sustainable ammonia production, *Joule* 5 (2021) 290–294, <https://doi.org/10.1016/j.joule.2020.12.025>.
- [29] Y. Guo, R. Zhang, S. Zhang, Y. Zhao, Q. Yang, Z. Huang, B. Dong, C. Zhi, Pd doping-weakened intermediate adsorption to promote electrocatalytic nitrate reduction on  $TiO_2$  nanoarrays for ammonia production and energy supply with zinc–nitrate batteries, *Energy Environ. Sci.* 14 (2021) 3938–3944, <https://doi.org/10.1039/dlee0086d>.
- [30] X. Fu, X. Zhao, X. Hu, K. He, Y. Yu, T. Li, Q. Tu, X. Qian, Q. Yue, M.R. Wasielewski, Y. Kang, Alternative route for electrochemical ammonia synthesis by reduction of nitrate on copper nanosheets, *Appl. Mater. Today* 19 (2020), 100620, <https://doi.org/10.1016/j.apmt.2020.100620>.
- [31] J.Y. Zhu, Q. Xue, Y.Y. Xue, Y. Ding, F.M. Li, P. Jin, P. Chen, Y. Chen, Iridium nanotubes as bifunctional electrocatalysts for oxygen evolution and nitrate reduction reactions, *ACS Appl. Mater. Interfaces* 12 (2020) 14064–14070, <https://doi.org/10.1021/acsmi.0c01937>.
- [32] Y. Feng, H. Yang, Y. Zhang, X. Huang, L. Li, T. Cheng, Q. Shao, Te-doped Pd nanocrystal for electrochemical urea production by efficiently coupling carbon dioxide reduction with nitrite reduction, *Nano Lett.* 20 (2020) 8282–8289, <https://doi.org/10.1021/acs.nanolett.0c03400>.
- [33] C. Lv, L. Zhong, H. Liu, Z. Fang, C. Yan, M. Chen, Y. Kong, C. Lee, D. Liu, S. Li, J. Liu, L. Song, G. Chen, Q. Yan, G. Yu, Selective electrocatalytic synthesis of urea with nitrate and carbon dioxide, *Nat. Sustain.* 4 (2021) 868–876, <https://doi.org/10.1038/s41893-021-00741-3>.
- [34] N. Meng, Y. Huang, Y. Liu, Y. Yu, B. Zhang, Electrosynthesis of urea from nitrite and  $CO_2$  over oxygen vacancy-rich  $ZnO$  porous nanosheets, *Cell Rep. Phys. Sci.* 2 (2021), 100378, <https://doi.org/10.1016/j.xcrp.2021.100378>.
- [35] Z. Wang, B. Richards, N. Singh, Recent discoveries in the reaction mechanism of heterogeneous electrocatalytic nitrate reduction, *Catal. Sci. Technol.* 11 (2021) 705–725, <https://doi.org/10.1039/docy02025g>.
- [36] J. Lim, C.-Y. Liu, J. Park, Y.-H. Liu, T.P. Senftle, S.W. Lee, M.C. Hatzell, Structure sensitivity of Pd facets for enhanced electrochemical nitrate reduction to ammonia, *ACS Catal.* 11 (2021) 7568–7577, <https://doi.org/10.1021/acscatal.1c01413>.
- [37] Y. Wang, C. Wang, M. Li, Y. Yu, B. Zhang, Nitrate electroreduction: mechanism insight, in situ characterization, performance evaluation, and challenges, *Chem. Soc. Rev.* 50 (2021) 6720–6733, <https://doi.org/10.1039/dics00116g>.
- [38] J. Li, G. Zhan, J. Yang, F. Quan, C. Mao, Y. Liu, B. Wang, F. Lei, L. Li, A.W.M. Chan, L. Xu, Y. Shi, Y. Du, W. Hao, P.K. Wong, J. Wang, S.X. Dou, L. Zhang, J.C. Yu, Efficient ammonia electrosynthesis from nitrate on strained ruthenium nanoclusters, *J. Am. Chem.* 142 (2020) 7036–7046, <https://doi.org/10.1021/jacs.0c00418>.
- [39] D.P. Butcher, A.A. Gewirth, Nitrate reduction pathways on Cu single crystal surfaces: effect of oxide and  $Cl^-$ , *Nano Energy* 29 (2016) 457–465, <https://doi.org/10.1016/j.nanoen.2016.06.024>.
- [40] H. Liu, J. Park, Y. Chen, Y. Qiu, Y. Cheng, K. Srivastava, S. Gu, B.H. Shanks, L. T. Roling, W. Li, Electrocatalytic nitrate reduction on oxide-derived silver with tunable selectivity to nitrite and ammonia, *ACS Catal.* 11 (2021) 8431–8442, <https://doi.org/10.1021/acscatal.1c01525>.
- [41] L. Wei, D.-J. Liu, A.B. Rosales, J.W. Evans, J. Vela, Mild and selective hydrogenation of nitrate to ammonia in the absence of noble metals, *ACS Catal.* 10 (2020) 3618–3628, <https://doi.org/10.1021/acscatal.9b05338>.
- [42] Q. Yao, J. Chen, S. Xiao, Y. Zhang, X. Zhou, Selective electrocatalytic reduction of nitrate to ammonia with nickel phosphide, *ACS Appl. Mater. Interfaces* 13 (2021) 30458–30467, <https://doi.org/10.1021/acsmi.0c22338>.
- [43] S. Xu, D.C. Ashley, H.Y. Kwon, G.R. Ware, C.H. Chen, Y. Losovjy, X. Gao, E. Jakubikova, J.M. Smith, A flexible, redox-active macrocycle enables the electrocatalytic reduction of nitrate to ammonia by a cobalt complex, *Chem. Sci.* 9 (2018) 4950–4958, <https://doi.org/10.1039/c8sc00721g>.
- [44] D. Zhang, B. Wang, X. Gong, Z. Yang, Y. Liu, Selective reduction of nitrate to nitrogen gas by novel  $Cu_2O$ – $Cu^0$ – $Fe^0$  composite combined with  $HCOOH$  under UV radiation, *Chem. Eng. J.* 359 (2019) 1195–1204, <https://doi.org/10.1016/j.cej.2018.11.058>.
- [45] X. Zhao, K. Zhao, X. Quan, S. Chen, H. Yu, Z. Zhang, J. Niu, S. Zhang, Efficient electrochemical nitrate removal on Cu and nitrogen doped carbon, *Chem. Eng. J.* 415 (2021), 128958, <https://doi.org/10.1016/j.cej.2021.128958>.
- [46] G.-F. Chen, Y. Yuan, H. Jiang, S.-Y. Ren, L.-X. Ding, L. Ma, T. Wu, J. Lu, H. Wang, Electrochemical reduction of nitrate to ammonia via direct eight-electron transfer using a copper–molecular solid catalyst, *Nat. Energy* 5 (2020) 605–613, <https://doi.org/10.1038/s41560-020-0654-1>.

[47] Y. Xu, M. Wang, K. Ren, T. Ren, M. Liu, Z. Wang, X. Li, L. Wang, H. Wang, Atomic defects in porhole-rich two-dimensional copper nanoplates triggering enhanced electrocatalytic selective nitrate-to-ammonia transformation, *J. Mater. Chem. A* 9 (2021) 16411–16417, <https://doi.org/10.1039/dta04743d>.

[48] Y. Wang, W. Zhou, R. Jia, Y. Yu, B. Zhang, Unveiling the activity origin of a copper-based electrocatalyst for selective nitrate reduction to ammonia, *Angew. Chem. Int. Ed. Engl.* 59 (2020) 5350–5354, <https://doi.org/10.1002/anie.201915992>.

[49] Z. Chen, Y.-C. He, J.-H. Chen, X.-Z. Fu, R. Sun, Y.-X. Chen, C.-P. Wong, PdCu alloy flower-like nanocages with high electrocatalytic performance for methanol oxidation, *J. Phys. Chem. C* 122 (2018) 8976–8983, <https://doi.org/10.1021/acs.jpcc.8b01095>.

[50] Q. Wang, Y. Lei, D. Wang, Y. Li, Defect engineering in earth-abundant electrocatalysts for  $\text{CO}_2$  and  $\text{N}_2$  reduction, *Energy Environ. Sci.* 12 (2019) 1730–1750, <https://doi.org/10.1039/c8ee03781g>.

[51] W. Zhong, Z. Wang, N. Gao, L. Huang, Z. Lin, Y. Liu, F. Meng, J. Deng, S. Jin, Q. Zhang, L. Gu, Coupled vacancy pairs in Ni-doped CoSe for Improved electrocatalytic hydrogen production through topochemical deintercalation, *Angew. Chem. Int. Ed.* 59 (2020) 22743–22748, <https://doi.org/10.1002/anie.202011378>.

[52] Z. Xia, S. Guo, Strain engineering of metal-based nanomaterials for energy electrocatalysis, *Chem. Soc. Rev.* 48 (2019) 3265–3278, <https://doi.org/10.1039/c8cs00846a>.

[53] C. Lu, L. Qi, J. Yang, X. Wang, D. Zhang, J. Xie, J. Ma, One-pot synthesis of octahedral  $\text{Cu}_2\text{O}$  nanocages via a catalytic solution route, *Adv. Mater.* 17 (2005) 2562–2567, <https://doi.org/10.1002/adma.200501128>.

[54] J. Qu, D. Chen, N. Li, Q. Xu, H. Li, J. He, J. Lu, Construction of Pd-modified  $\text{NiCoO}_x$  hollow nanospheres with surface hydroxyls and oxygen vacancies for highly enhanced catalytic toluene oxidation activity, *ACS Sustain. Chem. Eng.* 8 (2020) 10581–10587, <https://doi.org/10.1021/acssuschemeng.0c03755>.

[55] A. Ruiz Puigdollers, P. Schlexer, S. Tosoni, G. Pacchioni, Increasing oxide reducibility: the role of metal/oxide interfaces in the formation of oxygen vacancies, *ACS Catal.* 7 (2017) 6493–6513, <https://doi.org/10.1021/acscatal.7b01913>.

[56] X. Wang, Z. Rui, Y. Zeng, H. Ji, Z. Du, Q. Rao, Synergetic effect of oxygen vacancy and Pd site on the interaction between Pd/Anatase  $\text{TiO}_2$  (101) and formaldehyde: a density functional theory study, *Catal. Today* 297 (2017) 151–158, <https://doi.org/10.1016/j.cattod.2017.06.037>.

[57] Y. Xu, K. Ren, T. Ren, M. Wang, S. Yu, Z. Wang, X. Li, L. Wang, H. Wang, Phosphorus-triggered modification of the electronic structure and surface properties of  $\text{Pd}_4\text{S}$  nanowires for robust hydrogen evolution electrocatalysis, *J. Mater. Chem. A* 8 (2020) 19873–19878, <https://doi.org/10.1039/dta07403a>.

[58] T.J. Wang, F.M. Li, H. Huang, S.W. Yin, P. Chen, P.J. Jin, Y. Chen, Porous Pd-PdO nanotubes for methanol electrooxidation, *Adv. Funct. Mater.* 30 (2020), 20000534, <https://doi.org/10.1002/adfm.202000534>.

[59] T. Ren, K. Ren, M. Wang, M. Liu, Z. Wang, H. Wang, X. Li, L. Wang, Y. Xu, Concave-convex surface oxide layers over copper nanowires boost electrochemical nitrate-to-ammonia conversion, *Chem. Eng. J.* 426 (2021), 130759, <https://doi.org/10.1016/j.cej.2021.130759>.

[60] L. Li, X. Chen, Y. Wu, D. Wang, Q. Peng, G. Zhou, Y. Li, Pd-Cu(2)O and Ag-Cu(2)O hybrid concave nanomaterials for an effective synergistic catalyst, *Angew. Chem. Int. Ed. Engl.* 52 (2013) 11049–11053, <https://doi.org/10.1002/anie.201303912>.

[61] L. Lu, X. Xu, J. Yan, F.N. Shi, Y. Huo, Oxygen vacancy rich  $\text{Cu}_2\text{O}$  based composite material with nitrogen doped carbon as matrix for photocatalytic  $\text{H}_2$  production and organic pollutant removal, *Dalton Trans.* 47 (2018) 2031–2038, <https://doi.org/10.1039/c7dt03835f>.

[62] X. Pang, H. Bai, Y. Zhao, L. Qu, D. Xu, J. Ding, W. Fan, W. Shi, Photoelectrochemical detection of 4-nitrophenol by sensitive  $\text{Ni}/\text{Cu}_2\text{O}$  photocathode, *Electrochim. Acta* 367 (2021), 137453, <https://doi.org/10.1016/j.electacta.2020.137453>.

[63] R. Yang, X. Lu, X. Huang, Z. Chen, X. Zhang, M. Xu, Q. Song, L. Zhu, Bi-component  $\text{Cu}_2\text{O}-\text{CuCl}$  composites with tunable oxygen vacancies and enhanced photocatalytic properties, *Appl. Catal. B Environ.* 170–171 (2015) 225–232, <https://doi.org/10.1016/j.apcatb.2015.01.046>.

[64] R. Jia, Y. Wang, C. Wang, Y. Ling, Y. Yu, B. Zhang, Boosting selective nitrate electroreduction to ammonium by constructing oxygen vacancies in  $\text{TiO}_2$ , *ACS Catal.* 10 (2020) 3533–3540, <https://doi.org/10.1021/acscatal.9b05260>.

[65] S. Lv, Y. Wang, Y. Zhou, Q. Liu, C. Song, D. Wang, Oxygen vacancy stimulated direct Z-scheme of mesoporous  $\text{Cu}_2\text{O}/\text{TiO}_2$  for enhanced photocatalytic hydrogen production from water and seawater, *J. Alloy. Compd.* 868 (2021), 159144, <https://doi.org/10.1016/j.jallcom.2021.159144>.

[66] Y. Xu, T. Ren, K. Ren, S. Yu, M. Liu, Z. Wang, X. Li, L. Wang, H. Wang, Metal-organic frameworks-derived Ru-doped  $\text{Co}_2\text{P}/\text{N}$ -doped carbon composite nanosheet arrays as bifunctional electrocatalysts for hydrogen evolution and urea oxidation, *Chem. Eng. J.* 408 (2021), 127308, <https://doi.org/10.1016/j.cej.2020.127308>.

[67] Y. Xu, X. Chai, T. Ren, S. Yu, H. Yu, Z. Wang, X. Li, L. Wang, H. Wang, Ir-doped Ni-based metal-organic framework ultrathin nanosheets on Ni foam for enhanced urea electro-oxidation, *Chem. Commun.* 56 (2020) 2151–2154, <https://doi.org/10.1039/c9cc09484a>.

[68] Y. Xu, M. Liu, M. Wang, T. Ren, K. Ren, Z. Wang, X. Li, L. Wang, H. Wang, Methanol electroreforming coupled to green hydrogen production over bifunctional NiIr-based metal-organic framework nanosheet arrays, *Appl. Catal. B Environ.* 300 (2022), 120753, <https://doi.org/10.1016/j.apcatb.2021.120753>.

[69] K. Chu, F. Liu, J. Zhu, H. Fu, H. Zhu, Y. Zhu, Y. Zhang, F. Lai, T. Liu, A general strategy to boost electrocatalytic nitrogen reduction on perovskite oxides via the oxygen vacancies derived from A-site deficiency, *Adv. Energy Mater.* 11 (2021), 2003799, <https://doi.org/10.1002/aenm.202003799>.

[70] Y. Xu, K. Ren, T. Ren, M. Wang, M. Liu, Z. Wang, X. Li, L. Wang, H. Wang, Cooperativity of Cu and Pd active sites in CuPd aerogels enhances nitrate electroreduction to ammonia, *Chem. Commun.* 57 (2021) 7525–7528, <https://doi.org/10.1039/d1cc02105b>.

[71] C. Chen, H. Zhang, K. Li, Q. Tang, X. Bian, Jn Gu, Q. Cao, L. Zhong, C.K. Russell, M. Fan, J. Jia,  $\text{Cu}^{+}$  based active sites of different oxides supported Pd-Cu catalysts and electrolytic in-situ  $\text{H}_2$  evolution for high-efficiency nitrate reduction reaction, *J. Catal.* 392 (2020) 231–243, <https://doi.org/10.1016/j.jcat.2020.10.012>.

[72] W. Fu, Z. Hu, Y. Zheng, P. Su, Q. Zhang, Y. Jiao, M. Zhou, Tuning mobility of intermediate and electron transfer to enhance electrochemical reduction of nitrate to ammonia on  $\text{Cu}_2\text{O}/\text{Cu}$  interface, *Chem. Eng. J.* (2021), 133680, <https://doi.org/10.1016/j.cej.2021.133680>.

[73] G.A. Cerrón-Calle, A.S. Fajardo, C.M. Sánchez-Sánchez, S. García-Segura, Highly reactive Cu-P bimetallic 3D-electrocatalyst for selective nitrate reduction to ammonia, *Appl. Catal. B Environ.* 302 (2022), 120844, <https://doi.org/10.1016/j.apcatb.2021.120844>.